Journal of Materials Chemistry A

Dynamic Article Links▶

ARTICLE TYPE

Hybrid supercapacitor based on flower-like Co(OH)$_2$ and urchin-like VN electrode materials

Rutao Wang,[a,b,c]**Xingbin Yan,***[a,b]**Junwei Lang,**[a]**ZongminZheng**[a]**and PengZhang**[a]

A series of designed hybrid electrochemical capacitors have been firstly fabricated by using the flower-like cobalt hydroxide (Co(OH)$_2$) andurchin-like vanadium nitride (VN) as the positive and negative electrode materials, respectively. Both of Co(OH)$_2$ and VN electrode materials showed excellent
10 electrochemical performance due to their unique structure and fast reversible Faradic reaction characteristics. With the different operation voltage window (OVW) and negative/positive mass ratios, the impacts on capacitance performance of hybrid supercapacitor were investigated thoroughly, which demonstrated that both mass ratio and OVW played the important role on their capacitance performance. Furthermore, theoretical modeling was performed and the simulation result was in agreement with the
15 experimental results for the influence of negative/positive mass ratio on capacitance performance of hybrid supercapacitor. When an optimized negative/positive mass ratio was located 3, Co(OH)$_2$//VN hybrid supercapacitor could be cycled reversibly in the high-voltage region of 0-1.6 V and delivered an high energy density of 22 Wh kg^{-1}. Even at a large power density of 15.9 kW kg^{-1}, the hybrid supercapacitor still possessed a desirable specific energy density of 9 Wh kg^{-1}. Such an impressive hybrid
20 supercapacitor was expected to be a highly promising candidate for application in high-performance energy storage systems.

Introduction

Energy storage devices, in particular supercapacitors, have attracted considerable attention in future energy storage
25 applications.[1] Currently, supercapacitors have been widely used in consumer electronics, memory back-up systems, hybrid electrical vehicles and industrial power/energy management due to high power density (> 10 kW kg^{-1}), long cycle life (> 10^5 cycles) and fast charge/discharge processes (within seconds).[2-4]
30 However, they still suffer from a lower energy density compared with rechargeable batteries.[1,4] Therefore, it is urgent to develop advanced supercapacitors with enhanced energy density without sacrificing the power delivery and cycle stability to meet the future energy demands.
35 Aqueous hybrid supercapacitors, combining an energy-type Faradaic electrode and a power-type electrode, have been paid extensive attention as an alternative or supplement to batteries in energy storage field.[5-7] Aqueous electrolytes endow hybrid supercapacitor with the advantages of ionic conductivity, low
40 cost, non-flammability, environmentally robust, and easy to handle. Furthermore, the energy density of hybrid capacitor can increase through full use of the difference in the potential windows of two electrode materials to maximize operating voltage in the cell system.[8-10] Therefore, hybrid supercapacitorare
45 able to fill the gap between batteries and conventional capacitors without sacrificing energy/power delivery and cycle life.

Various electrode materials such carbon, transition metal oxides, metal hydroxides, and electronically conducing polymer materials have been widely investigated for potential applications
50 in hybrid supercapacitor.[5,6] Among that, studies on hybrid supercapacitor with metal oxides/hydroxides and activated carbon (AC) as positive and negative electrodes in aqueous electrolyte, respectively, are becoming the hot topic. AC based hybrid supercapacitor, such as PbO$_2$//AC,[11]NiO//AC,[12] Co(OH)$_2$//AC,[13]
55 Ni(OH)$_2$//AC,[14] MnO$_2$//AC,[15] MoO$_3$//AC,[16] Li insertion materials (LiMn$_2$O$_4$, LiNi$_{1/3}$Co$_{1/3}$Mn$_{1/3}$O$_2$, LiFe$_{0.5}$Mn$_{0.5}$PO$_4$, and LiFePO$_4$)//AC,[17-20] have been widely reported, and they all exhibit high work potential region of 1.2-2 V and much improved energy density ranging from 10 to 50 Wh kg^{-1}. For negative
60 materials aspect, AC is characterized by a high hydrogen evolution overpotential, considerable specific capacitance, and impressive rate capability. However, the low volume density and high surface area (> 1000 m^2/g) of AC limit the volume energy performance in this hybrid supercapacitor system.[21-23]This is
65 majorly attributed to the increased volume percentage of the

negative electrode and extra electrolyte within these hybrid supercapacitors. Therefore, it is necessary to explore other electro-active negative materials with a large specific capacitance instead of the activated carbon to form a hybrid cell.

5 To our knowledge, only a few of metal oxides are considered to the qualified candidates as the negative electrode materials in hybrid supercapacitors, such as RuO_2,[24] $FeOOH$,[25] MoO_3,[26] V_2O_5,[27] TiO_2,[28] and $MnFe_2O_4$.[29] RuO_2 is the most prominent negative materials due to its considerable electrical conductivity

10 and high specific capacitance, however, the high cost of Ru is a limitation for practical application. Though $FeOOH$ and $MnFe_2O_4$ can be used as negative materials for hybrid supercapacitors, the hybrid systems are suffer from their low energy and power delivery. Metal nitride, especially vanadium nitride (VN), is

15 considered to be good candidates as negative materials in hybrid supercapacitor due to their large theoretical capacity (> 500 F g^{-1}), reversible and fast redox Faradic response, and high hydrogen evolution overpotential.[30,31] Up to now, there are rare reports on VN based hybrid supercapacitors only of $V_2O_5//VN$ and $NiO//VN$

20 systems.[21,23,32] Considerable energy density and power delivery can be achieved in these VN based hybrid systems, which is comparable to AC based hybrid supercapacitors.

Herein, we have successfully designed a series of hybrid supercapacitor consisting of the urchin-like VN negative and

25 flower-like $Co(OH)_2$ positive electrode materials. The experimental and theoretical results prove that the negative/positive mass ratio plays an important role in determining the capacitance of $Co(OH)_2//VN$ hybrid supercapacitor. The optimal hybrid supercapacitor thus shows a

30 high energy density of 22 Wh kg^{-1} at a power density of 0.16 kW kg^{-1}, and a high power density of 15.9 kW kg^{-1} at an energy density of 9 Wh kg^{-1}, all with a 1.6 V cell voltage operating in 2 M KOH aqueous electrolyte. This strategy for the choice of metal oxide or nitride provided a promising route for new-type

35 supercapacitor with high energy and power densities.

Experimental section

2.1 Synthesis of flower-like $Co(OH)_2$

Flower-like $Co(OH)_2$ was synthesized by a facile precipitation method. In a typical experiment, 0.01 M of $CoCl_2 \cdot 6H_2O$ was

40 dissolved in 10 ml of distilled water under magnetic stirring. NH_4OH solution (5 wt.%) was slowly added into the $CoCl_2 \cdot 6H_2O$ solution until the pH values reached 9. The reaction mixture was stirring vigorously for 3h at room temperature. Then the solid was filtered and washed with a copious amount of distilled water.

45 The obtained product was dried at a temperature of 60 °C in air for 12 h.

2.2 Synthesis of urchin-like VN

The urchin-like VN were firstly fabricated through a two-step approach. First, we used a modified method according to Lou'

50 work.[27] Typically, commercial V_2O_5 (4.8 g) and $H_2C_4O_4 \cdot H_2O$ in a molar ratio of 1:3 were dissolved in 160 ml of distilled water under vigorous stirring at 80 °C for 5 h. A blue clear solution (VOC_2O_4) was formed. 5 ml of VOC_2O_4 (about 0.33 M) solution was then added into a 50 ml Teflon container, followed by

55 addition of 1 ml of H_2O_2 (35 wt.%) under stirring. After 10 min, 15 ml of ethanol was added and the obtained solution was stirred

for another 5 min. Then the container was sealed in an autoclave and transferred to an electrical over and kept at 180 °C for 24 h. After cooling down naturally, the precipitates were collected by

60 filtering with distilled water for several times and dried at 60 °C for 12h. Second, as-made precipitate was directly annealed the in NH_3 (flow rate 40 cc min^{-1}) at 600 °C for 2 h with a heating rate of 5 °C min^{-1} to obtain the urchin-like VN micro-flowers.

2.3 Structural characterization

65 Field emission scanning electron microscopy (FESEM, JSM 6701F) and transmission electron microscopy (TEM, JEOL 2100 FEG) were employed to investigate the morphology and microstructure of as-prepared electrode materials. Powder X-ray diffraction (XRD, Rigaku D/Max-2400) was performed using Cu-

70 Kα radiation to investigate the structure and composition of the samples. The nitrogen adsorption-desorption isotherm measurements were performed on a Micromeritics ASAP 2020 volumetric adsorption analyzer at 77 K. The Brunauer-Emmett-Teller (BET) method was utilized to calculate the specific surface

75 area. The total pore volume was estimated from the amount adsorbed at a relative pressure of $P/P_0 = 0.99$.

2.4 Electrode preparation and electrochemical measurements.

The working electrodes were prepared as follows: 90 wt% of sample was mixed with 5 wt% of acetylene black in an agate

80 mortar until a homogeneous black powder was obtained. To this mixture, 5 wt% of poly(tetrafluoroethylene) was added with a few drops of ethanol. After briefly allowing the solvent to evaporate, the resulting paste was pressed at 10 MPa to the nickel gauze with a nickel wire for an electric connection. The

85 assembled electrodes were dried for 12 h at 60 °C in air. Each electrode contained about 5 mg of electro-active material and had a geometric surface area of about 1 cm^2.

Electrochemical measurements were performed using an electrochemical working station (CHI660D, Shanghai, China) in

90 a three-electrode system in 2 M KOH aqueous electrolyte at room temperature. A platinum gauze electrode and a saturated calomel electrode served as the counter electrode and the reference electrode, respectively. The average specific capacitance values were calculated from the galvanostatic discharge curves, using

95 the following equation:

$$C = I/[(dE/dt) \times m] \approx I/[(\Delta E/\Delta t) \times m](\text{F g}^{-1}) \quad (1)$$

Where I is constant discharge current, Δt is the time period for a full discharge, m indicates the mass of the corresponding active electrode material, and ΔE represents the voltage change after a

100 full discharge.

A two-electrode cell configuration was used to measure the performance of asymmetric supercapacitor in 2 M KOH aqueous electrolyte solution. The working electrodes were prepared by the as above-stated method. After drying, the two identical electrodes

105 were pressed at 10 MPa, and they were placed together and separated by a porous nonwoven cloth separator. And then, the assemble two-electrode cellwas infiltrated with 2 M KOH solution. Finally, the assemble two-electrode cell was sealed by plastic film and tightly clamped by two poly(tetrafluoroethylene)

110 plates. The energy density (E) of aqueous asymmetric supercapacitor can be achieved by the specific capacitance (C) and the cell voltage (V) according to the following equation:

$$E = 0.5 \, CV^2 \quad (2)$$

The power density (*P*) of asymmetric supercapacitor can be achieved by the energy density (*E*) and the discharging time (*t*) according to the following equation:

$$P = E/t \quad (3)$$

5 Results and discussion

3.1 Flower-like Co(OH)₂ positive materials

The typical low-magnification scanning electron microscope (SEM) image (Fig. 1a) clearly illustrates that the as-synthesized Co(OH)₂ samples are composed of many well-defined
10 microflowers with interconnected nanoflakes. The high-magnification SEM image (Fig. 1a inset) reveals that these nanoflakes have the ultrathin structure with the thickness below 10 nm. The TEM image (Fig. 1b) also proves the flower-like structure of as-synthesized Co(OH)₂ which composed of
15 interconnected and ultrathin nanoflakes. In the corresponding selected-area electron-diffraction pattern (Fig. 1b inset), the broad and diffused halo rings are observed, indicating an polycrystalline structure of Co(OH)₂ flowers. No sharp peaks have been observed in the powder X-ray diffraction (XRD) pattern (Fig. 1c),
20 and which is corresponding to the layered α-Co(OH)₂ structure (PDF, card no. 46-0605) with low crystallinity. Furthermore, the profile of the adsorption-desorption hysteresis loop is characteristic of porous structure for the layered α-Co(OH)₂ (Fig. 1d). The wide capillary condensation step toward higher relative
25 pressure indicates the wide distribution of pore sizes, which can also be observed in the Barrett-Joyner-Halenda (BJH) mesopore-size-distribution curves. The Brunauer-Emmet-Teller (BET) specific surface area of as-synthesized Co(OH)₂ are calculated to be 85 m² g⁻¹ along with a large pore volume of 0.33 cm³ g⁻¹. Such
30 flower-like structure of Co(OH)₂ could benefit the penetration of the electrolyte OH⁻ to Co(OH)₂ active material, which is crucial for surface redox reactions.

Electrochemical characterization of the specific pseudocapacitance of porous Co(OH)₂ hydroxides microflowers
35 were investigated by cyclic voltammetry (CV) and galvanostatic test in a three-electrode beaker cell with a 2 M KOH electrolyte. The typical pseudocapacitive behavior of flower-like Co(OH)₂ is present in the form of one pair of strong redox peaks in CV curves (Fig. 2a). The redox peaks of CV curves correspond to the
40 conversion between different cobalt oxidation states. The two sequential reactions are described as follows:[13,33]

$$Co(OH)_2 + OH^- \leftrightarrow CoOOH + H_2O + e^-$$
$$CoOOH + OH^- \leftrightarrow CoO_2 + H_2O + e^-$$

The capacitive response comes from as above-stated Faradic
45 redox reactions, which is very distinct from that of electric double layer capacitors that commonly produce a CV curve close to an ideal rectangular shape. Fig. 2b shows the galvanostatic charge/discharge curves at the different current densities. The observation of nearly symmetric potential-time curves at all
50 current densities implies the high charge-discharge columbic efficiency and low polarization of our electrode. The specific capacitance values calculated from the discharge curves are 429, 405, and 369 F g⁻¹ at the current densities of 1, 2, and 5 A g⁻¹, respectively, as shown in Fig. 2c. Even at a relatively high current
55 density of 10 A g⁻¹, the specific capacitance is still maintained at
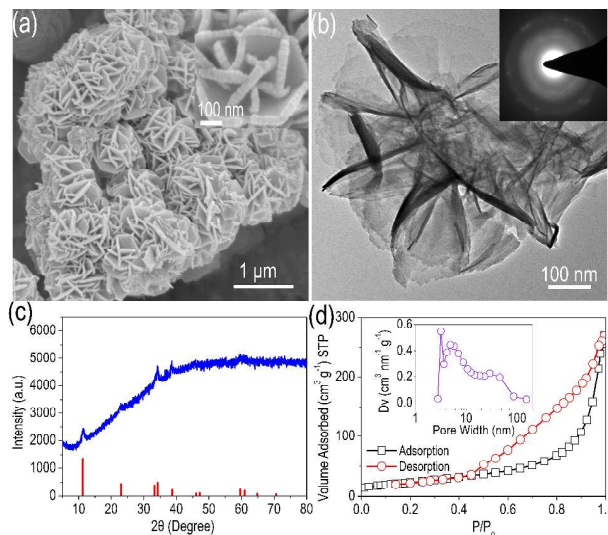
Fig.1 Morphology and structure characterization of flower-like Co(OH)₂:
(a) SEM images and high-resolution SEM images in inset, (b) TEM images of Co(OH)₂, inset images showing the selected area electron
60 diffraction (SAED), (c) XRD pattern, (d) the N₂ sorption isotherms and the pore size distribution (inset) of flower-like Co(OH)₂
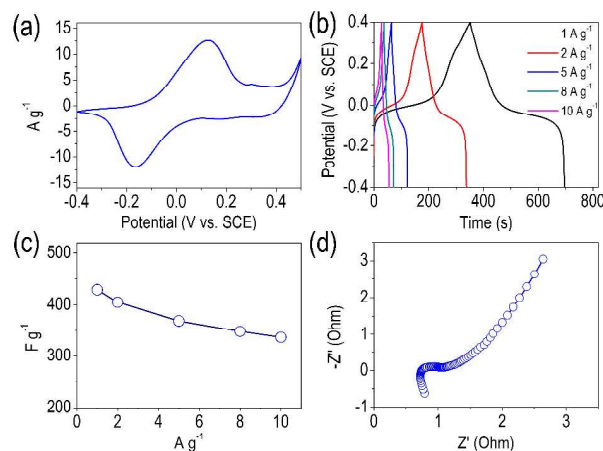
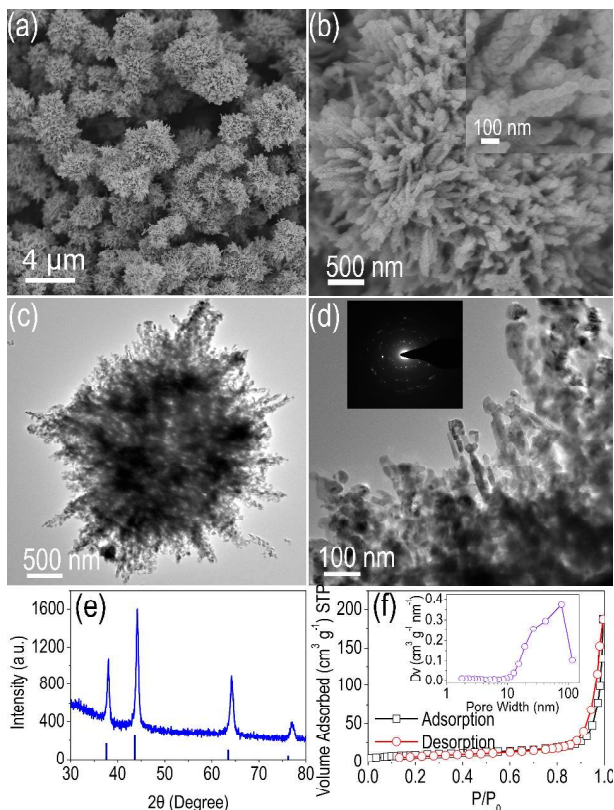

Fig.2 Electrochemical characteristics of flower-like Co(OH)₂ in 2M KOH electrolyte under a three-electrode system: (a) typical CV curve at the
65 scan rate of 10 mV s⁻¹, (b) galvanostatic charge/discharge curves at different current densities, (c) the specific capacitance as a function of the discharge current density, and (d) Nyquist plot showing the imaginary part versus the real part of impedance

337 F g⁻¹, thereby exhibiting the high capacitance performance
70 and good rate capability of flower-like Co(OH)₂. The Nyquist plot (Fig. 2d) ranging from 100 kHz to 0.01 Hz features a high phase-angle (exceeding 45°) impedance plot and a low Faradic charge transfer resistance, indicating the fast ion transfer behavior of flower-like Co(OH)₂.

75 3.2 Urchin-like VN negative materials

As shown in Fig. 3a and b, uniform urchin-like VN micro flowers with an average diameter of about 3-5 μm are composed of one-dimensional (1D) nanorods. High-resolution SEM image reveals that 1D nanorods with overall diameter of around 100 nm which
80 are composed of closely stacked nanoparticles with a diameter of around 20 nm. TEM image (Fig. 3c and 3d) also reveals the urchin-like morphology of VN microflowers. Selected area electron diffraction (SAED) pattern (Fig. 3d inset) shows that each diffraction spot is converted into an arc, which is the

Fig.3 Morphology and structure characterization of urchin-like Co(OH)$_2$: (a) and (b) SEM images and high-resolution SEM images in inset, (c) and (d) TEM images and the selected area electron diffraction (SAED, inset image), (e) XRD pattern of urchin-like VN, (f) the N$_2$ sorption isotherms and the pore size distribution (inset) of urchin-like VN.
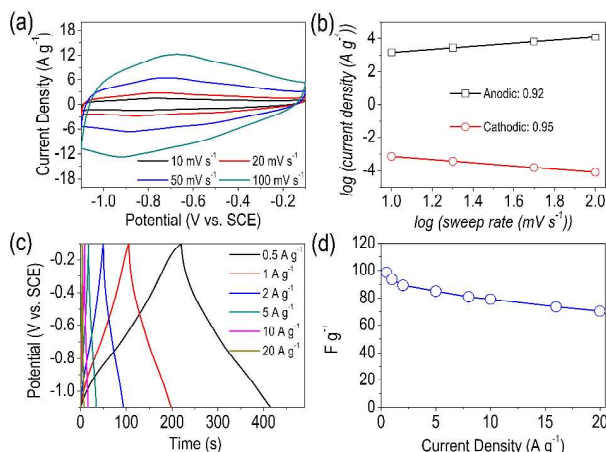
Fig.4 Electrochemical characteristics of urchin-like VN in 2M KOH electrolyte under a three-electrode system: (a) CV curves at the scan rates, (b) the relation between peak anodic (or cathodic) currents and CV scan rates, (c) galvanostatic charge/discharge curves at different current densities, and (d) the specific capacitance as a function of the discharge current density

evidence of texture in the polycrystalline structure. The urchin-like VN can be interpreted as porous nanorods which built with interconnected nanoparticles. XRD analysis (Fig. 3e) proves that porous VN microflowers are cubic-phase crystallize where the calculated crystallite size is about 14.3 nm. The porosity of the VN microflowers is also verified by N$_2$-sorption isotherm measurement. Fig. 3f shows that porous VN microflowers exhibit

a typical type-IV isotherm, characteristic of mesoporous structure with the measured BET specific surface area of 34 m^2 g^{-1}. The pore size distribution of VN is shown in Fig. 3f inset. It is dominated mostly by pores in the range of 20-100 nm.

The electrochemical properties of urchin-like VN electrodes are evaluated by CV and galvanostatic test. Fig. 4a shows the typical CV curves collected in a potential window between -0.1 V and -1.1 V at different scan rates. Even the working potential decreases to -1.2 V, no obvious polarization current is observed (Fig. S1). In all CV curves, two broad redox humps during the anodic (-0.8 V to -0.6 V) and cathodic (-1 V to -0.8 V) scans and the widecurrent-potential response can be observed, indicated that capacitive mechanism of VN electrode is composed of redox pseudocapacitance and electrical double layer capacitance. It is widely recognized that an oxide layerpresented on the VN surface, the following redox reaction of VN in aqueous KOH electrolyte can be proposed:[34-36]

$$VN_xO_y + OH^- \leftrightarrow VN_xO_y//OH^- + VN_xO_y\text{-}OH$$

Where VN$_x$O$_y$//OH$^-$ and VN$_x$O$_y$-OH correspond to the electrical doublelayer and redox reaction, respectively. The CV curves present essentially the same shape as the scan rate increase from 10 to 100 mV s^{-1}, indicating the good capacitive behavior of VN microflowers. Fig. 4b presents a plot of *log(i)*verus*log(v)* from 10 to 100 mV s^{-1} for both cathodic and anodic peaks. To sweep rates ranging from 10 to 100 mV s^{-1}(corresponding to charging times < 100 s), the slope values for both the cathodic and anodic peaks are 0.92 and 0.95, respectively, which indicate the kinetics are majorly surface-controlled, and thus fast. As shown in Fig. 4c the charge-discharging curves are almost linear and show a typical triangular symmetrical distribution, displaying perfect reversibility of the pseudocapacitive reactions for VN in 2 M KOH aqueous electrolyte. The specific capacitance is 98.5 F g^{-1} at the current density of 0.5 A g^{-1} (Fig. 4d). Furthermore, VN electrode exhibits excellent rate capability, and the retention rate of VN is 71.6 % when the discharging current density increases from 0.5 to 20 A g^{-1}, which is higher than other VN nanoparticles and still comparable to other VN nanostructures.[21,23,34,35] The superior electrochemical performance of VN microflowers can be attributed to the porous structure with large accessible surface area.

**3.3 Hybrid supercapacitor based on flower-like Co(OH)$_2$ and urchin-like VN**

Considering the high pseudocapacitance of flower-like Co(OH)$_2$ and the excellent rate capability of the urchin-like VN, VN/Co(OH)$_2$ hybrid supercapacitor was fabricated as shown in Fig. 5a. Fig. 5b show that the VN electrode was measured at a scan rate of 20 mV s^{-1} with a potential window of -0.1 V to -1.2 V (vs. SCE), while Co(OH)$_2$ was measured within a potential window of -0.4 V to +0.5 V (vs. SCE). By expressing the total cell voltage as the sum of the potential range of VN and Co(OH)$_2$, the hybrid supercapacitor can be operated up to 1.6 V. When the hybrid supercapacitor work with in a potential range of 0-1.6 V, it can reach a safe performance of both electrodes during long cycling.Fig. 5c exhibits the CV curves of the optimized hybrid supercapacitor (VN/Co(OH)$_2$ mass ratio: 3) measured at different scan rates of 5, 10, 20, 50, and 100 mV s^{-1} between 0 and 1.6 V in2 M KOH solutions. A couple of symmetric redox peaks, derived from the fast redox reactions on the VN and Co(OH)$_2$
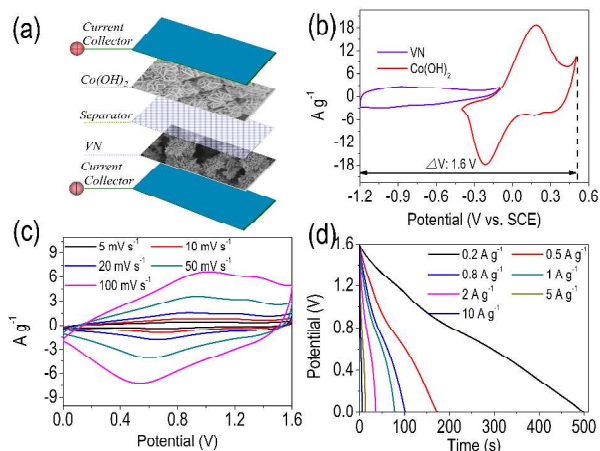
Fig.5 (a) Schematic of the assembled structure of hybrid supercapacitor based on the flower-like $Co(OH)_2$ as the positive electrode and urchin-like VN as the negative electrode. (b) Cyclic voltammetry profiles for $Co(OH)_2$ and VN electrode recorded at 20 mV s^{-1} in a three electrode cell in 2 M KOH electrolyte. Electrochemical characteristics of as-fabricated hybrid supercapacitor: (c) CV curve at the different scan rates, (d) galvanostatic discharging curves at the different current densities.

microflower electrode, are observed in each CV curves even at the high scan rates. The shapes of all these curves are almost the same, indicating the excellent rate capability of as-fabricated hybrid supercapacitor. The high specific capacitance and rate capability of the hybrid supercapacitor are revealed by galvanostatic measurements (Fig. 5c). The specific capacitance is 62.4 F g^{-1} at a current density of 0.2 A g^{-1}. At a high current density of 10 A g^{-1}, a useful capacitance of 34.4 F g^{-1} is measured. The high performance of our hybrid supercapacitor can be attributed to the individual properties of electrode materials andtheir synergistic effects between the positive and negative electrodes. Both $Co(OH)_2$ and VN are pseudo-capacitive materials with high theoretical specific capacitance values. The micro-flower morphology and porous structure of $Co(OH)_2$ and VN are able to enrich in electrolyte ions and shorten the diffusion paths for both electrons and ions, resulting in the increase of specific capacitance and rate capability of hybrid supercapacitor. In addition, operation voltage window (OVW) and mass ratio of $Co(OH)_2$/VN play the important roles in enhancing the electrochemical properties of hybrid supercapacitor—as demonstrated below.

In a control experiment, an $Co(OH)_2$//VN hybrid supercapacitor with mass ratio of 3 works at different potential windows in 2 M KOH aqueous solution at a scan rate of 50 mV s^{-1} as shown in Fig. 6a. When OVW is located at 1.0 V, a triangular CV curve implies an incomplete pseudocapacitive response from the hybrid supercapacitor. By increasing the OVW to 1.2 V, oxidation and reduction humps appear in the CV curves, showing the pseudo-capacitive properties.Further increased OVW to 1.6 V, some distinct redox peaks arise in these CV curves, indicating the moredeep redox reactions on the surface of positive $Co(OH)_2$ and negative VN electrode. Fig. 6b shows the galvanostatic charge-discharge curves under the different OVWs ranging from 1.0 V to 1.6 V at the current density of 1 A g^{-1}. It can be clearly seen that as-fabricated hybrid supercapacitor shows a good capacitive behavior with quasi-symmetrical triangular charge-discharge curves, even at voltages up to 1.6 V. Fig. 6b(inset image) depicts
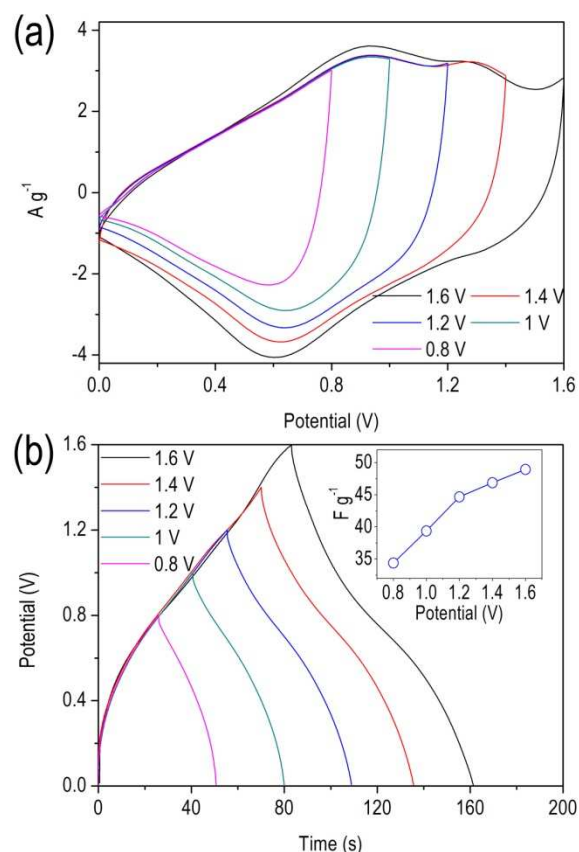
**Fig.6** (a) CV (scan rate of 50 mV s^{-1}) and (b) galvanostatic charge/discharge curves (current density of 1 A g^{-1}) of an optimized $Co(OH)_2$//VN hybrid supercapacitor (VN/$Co(OH)_2$ mass ratio: 3) measured at different potential windows in 2 M KOH electrolyte, inset image in (b) showing the specific capacitance of the hybrid supercapacitor with the increase of potential window at the current density of 1 A g^{-1}.

the specific capacitance of the hybrid supercapacitor as a function of the OVW and discharging time. It is found that the specific capacitance increase from 34.4 F g^{-1} to 48.9 F g^{-1} as the OVW range increases from 1.0 V to 1.6 V, but there is no significant change in internal resistance (from IR drop, Fig. S2). It means that the stored energy and delivered power density could be improved at least by 263%, according to equation 2 and 3. The capacitance performance of VN/$Co(OH)_2$ hybrid supercapacitor improves gradually with the elevated OVW, which is related to the continually in-depth redox reactions of electrode materials from less to more.[12,21]The OVW range of hybrid supercapacitor is higher than that of symmetrical supercapacitor fabricated by VN (Fig. S8) or $Co(OH)_2$-based electrodes (less than 1.2 V, Fig. S9). When the optimal OVW of 1.6 V is selected, the overall performance of the hybrid supercapacitor could be remarkably improved in 2 M KOH aqueous electrolyte.

In order to further develop an optimal VN/$Co(OH)_2$ hybrid supercapacitor, the charges at positive (q_+) and negative (q-) electrodes should be balanced ($q_+ = q_-$). The charge stored by each electrode depends on the specific capacitance (C), the charge/discharge potential range (V) and the mass electrode (m) following Equation 4:[7,8]

$q = C \times V \times m$ (4)

In order to obtain $q_- = q_+$, it is necessary to balance the mass ratio between the two electrodes. The mass balancing will be
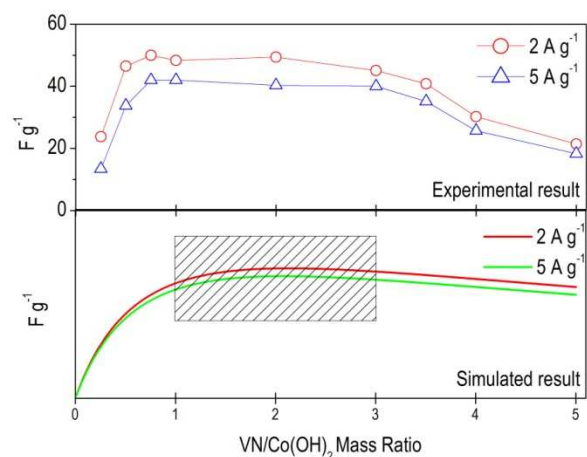
Fig.7 Plots of specific capacitance with VN/Co(OH)$_2$ mass ratio of hybrid supercapacitor from experimental results and simulated results from Wilson' mathematical model. The shadow area shows the maximum specific capacitance area of hybrid supercapacitor

expressed as follows:

$$m_- / m_+ = (C_+ \times V_+)/(C_- \times V_-) \qquad (5)$$

Based on C and V for Co(OH)$_2$ and VN micro-flowers, the optimal mass ratio between the negative and positive electrodes should be m$_{VN}$/m$_{Co(OH)2}$ = 3.6. Whether the mass ratio (m$_{VN}$/m$_{Co(OH)2}$: 3.6) is a optimal choice decided by equation (5). Recently, Zheng and Wilson *et al.* predicted that the maximum electrochemical capacitive value was obtained at the low positive/negative mass ratio (less than the q balance value) through two types of mathematical models.[37-39] In order to determine the optimal VN/Co(OH)$_2$ mass ratio, hybrid supercapacitors was fabricated by using different negative/positive mass ratio, 0.25, 0.5, 0.75, 1, 2, 3, 3.5, 4, and 5. Fig. S3 shows that the CV curves of hybrid supercapacitors under the different mass ratios. Interestingly, under the low VN/Co(OH)$_2$ mass ratios (below 2), the CV profiles of the as-fabricated supercapacitor show the quasi-rectangular shapes at the low voltage range. The quasi-rectangular shape may be related to the incomplete redox reaction of the Co(OH)$_2$ electrode. However, significant increment in the positive current (positive polarization) at the high voltage is noticed. This may be due to imbalanced q between Co(OH)$_2$ and VN electrode leads to H$_2$ evolution at the negative VN electrode. Nevertheless, the degree of positive polarization falls gradually as the increment of VN/Co(OH)$_2$ mass ratio. Less positive polarization is found at the high VN/Co(OH)$_2$ mass ratio. As the VN/Co(OH)$_2$ mass ratios of hybrid supercapacitor over 2, a pair of redox humps arise near the 0.8 V. Especially, an obvious redox peaks appears under the high VN/Co(OH)$_2$ mass ratio of 5, which indicates a battery-like behavior dominates in this hybrid cell.

Fig. S4 show the typical galvanostatic charge-discharge curves of hybrid supercapacitors under the different VN/Co(OH)$_2$ mass ratios. At the low VN/Co(OH)$_2$ mass ratios (below 1), a non-capacitive behavior with asymmetric charge-discharge lines is found around 1.2-1.6 V, indicating the low columbic efficiency of hybrid supercapacitor. This behavior is probably related with the fact that hydrogen produced during the negative polarization of the VN electrode. The non-symmetric charge-discharge lines gradually disappeared with the increase of the VN/Co(OH)$_2$ mass
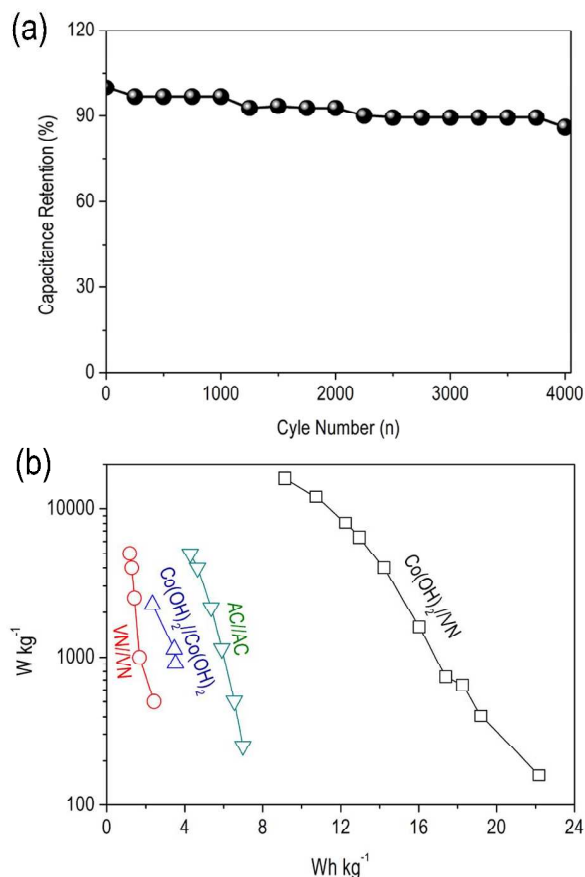
Fig.8 Plot of cycle stability of Co(OH)$_2$//VN hybrid supercapacitor with the VN/Co(OH)$_2$ mass ratio of 3 at the current load of 1 A g^{-1}.(b) Ragone plot (power density vs. energy density) of hybrid supercapacitor made of Co(OH)$_2$ and VN. Comparison of supercapacitor composed of VN//VN, Co(OH)$_2$//Co(OH)$_2$, and commercial AC//AC (AC from *ShiheziTianfu Tech Co., Ltd,China*).

ratio. When the VN/Co(OH)$_2$ mass ratio is set to or over 3, a symmetric charge-discharge line can be obtained. However, oversized VN mass (VN/Co(OH)$_2$ mass ratio over 4) in the negative electrode leads to the discharge line distort. Fig. S5 shows the specific capacitance values of hybrid capacitors at the different discharging current densities. The rate capability of hybrid supercapacitors increases at the higher VN/Co(OH)$_2$ mass ratio, which indicate that more VN addition is in favor of the reducing over current and improving the efficiency of charge-discharge. It is worth noting that the higher specific capacitance values of hybrid capacitors can be obtained at the lower VN/Co(OH)$_2$ mass ratios (0.75-3). Fig. S6 shows the cycle stabilities of the hybrid supercapacitor under the different VN/Co(OH)$_2$ mass ratios. A stable cycling stability (> 80% of initial capacitance after 4000 cycles) can be obtained as the VN/Co(OH)$_2$ mass ratio is over to 2, which suggests that a gravimetrically oversized VN negative electrode is possibly to extend the hybrid supercapacitor cycle-life by reducing the swing potential across the positive electrode.

Furthermore, we used the Wilson' mathematical model to find the region of optimal positive/negative mass ratio which corresponded to the maximum capacitive value of hybrid supercapacitor (more details in *reference 39* and supporting information). Simulation result (Fig. 6 and Fig. S7) suggests that

the higher capacitive performance can be obtained at the lower range of VN/Co(OH)$_2$ mass ratios about 1-3, which is approaching to the our experimental results (about 0.75-3). Especially, the highest capacitive performance of hybrid supercapacitor can be obtained as the VN/Co(OH)$_2$ mass ratio is about 2. This value is less than the optimal mass ratio about 3.6 calculated from equation 5. The different is attributed to that Wilson' mathematical model is not considered to the positive and negative swing voltages.[39]

In our experimental results, the higher capacitance can be obtained at VN/Co(OH)$_2$ mass ratios about 0.75-3. The low VN percentage in total hybrid capacitance can bring about the high capacitive performance. But the corresponding hybrid supercapacitors have the limited cycling stability, so far being well below expectations. As shown in Fig. S5, the hybrid capacitor with a VN/Co(OH)$_2$ mass ratio of 0.75 possesses the highest capacitance value of 88.3 F g^{-1} at 0.2 A g^{-1}, however, the capacitance value drops by 18% after only 1000 cycles. Under the lower VN/Co(OH)$_2$ mass ratios, the extra Faradic current from water splitting at the high OWV region (Fig. S3 and Fig. S4) can introduce the additional charges. These additional charges are included in the capacitance calculation and leads to the high but untrue capacitance values. As the VN/Co(OH)$_2$ mass ratio is 2, closer to the optimal mass ratio from simulated result, the corresponding hybrid supercapacitor shows a high capacitance value of 76.7 F g^{-1} and a relatively lower cycle-life about 71% of initial capacitance. At the hybrid capacitor with the mass ratio of 3.5, closer to the value calculated from equation 5, shows the high cycle stability (86.6% of initial capacitance value), whereas the capacitance value is down to 54.6 F g^{-1}.

Base on the stated above, the experimental and simulation results show that operating hybrid supercapacitor at the low optimal mass ratios can deliver the higher specific capacitance values but involve a trade-off in cycle-life. Under these conditions to obtain the maximum capacitance, severe redox reactions and fast voltage swing may occur in the positive Co(OH)$_2$ electrode, as well as the negative polarization from hydrogen evolution happens on the VN electrode. A gravimetrically oversized VN electrode can reduce the proportion of voltage swing across the positive electrode and eliminate the hydrogen evolution experienced at the negative electrode. This is well suited to long-term cycling, but will lead to a less-than-optimum specific capacitance value of the hybrid supercapacitor. Thus, considering the specific capacitance, OVW, and cycling stability, the optimal VN/Co(OH)$_2$ mass ratio of the hybrid supercapacitor is 3. Under the optimal mass ratio, hybrid supercapacitor has the specific capacitance of 62.4 F g^{-1}, a long cycling-life (86% of initial specific capacitance, Fig.8a), and the high rate capability, which is much higher than that of symmetrical Co(OH)$_2$//Co(OH$_2$), VN//VN, and the commercial AC//AC supercapacitor (Fig. S8-10). Importantly, the optimal hybrid supercapacitor exhibits a high energy density of 22 Wh kg^{-1} at a power density of 0.16 kW kg^{-1}, and a high power density of 15.9 kW kg^{-1} at an energy density of 9 Wh kg^{-1} (Fig. 8b).

Conclusions

A novel and durable asymmetric hybrid supercapacitor based on flower-like Co(OH)$_2$ and urchin-like VN materials as the positive and negative electrodes, respectively, has been fabricated in aqueous KOH electrolyte. After optimization of OWV and VN/Co(OH)$_2$ mass ratio, the as-assembled hybrid supercapacitor can be cycled reversibly in the voltage region of 0-1.6 V, and exhibits the maximum specific capacitance of 62.4 F g^{-1}. In addition, it delivers an energy density of 22 Wh kg^{-1} and has an excellent rate capability. Even at a power density of 15.9 kW kg^{-1}, it still has a specific energy of 9 Wh kg^{-1}. Moreover, the hybrid supercapacitor exhibits good long cycle-life along with 86% specific capacitance retained after 4000 cycles. This is the first time that Co(OH)$_2$ and VN electrode materials have been paired up to produce supercapacitors with excellent electrochemical performance. The impressive results presented here show great potential in designing new type of hybrid supercapacitor for promising applications in the high performance energy storage systems.

Acknowledgments

Notes and references

^{a} Laboratory of Clean Energy Chemistry and Materials, Lanzhou Institute of Chemical Physics, Chinese Academy of Science, Lanzhou 730000, P. R. China Fax: （+86）931 4968055; Tel: （+86）931 4968055; E-mail: xbyan@licp.cas.cn

^{b} State Key Laboratory of Solid Lubrication, Lanzhou Institute of Chemical Physics, Chinese of Academy of Sciences, Lanzhou, 730000, China

^{c} Graduate University of Chinese Academy of Sciences, Chinese of Academy of Sciences, Beijing, 100080, China

† Electronic Supplementary Information (ESI) available: [details of CV, charging/discharging, Ragone plot and cycle life curves of Co(OH)$_2$//VN hybrid supercapacitro with different mass ratio, Wilson' mathematical model, the electrochemical performance of VN//VN, AC//AC and Co(OH)$_2$//Co(OH)$_2$symetricalsupercapacitor].   See DOI: 10.1039/b000000x/

1   Y. Gogotsi and P. Simon, *Science*, 2011, **334**, 917.
2   A. G. Pandolfo and A. F. Hollenkamp, *J. Power Sources,* 2006, **157**, 11.
3   Y. Zhai, Y. Dou, D. Zhao, P. F. Fulvio, R. T. Mayes and S. Dai, *Adv. Mater.*, 2011, **22**, 4828.
4   B. Dunn, H. Kamath and J. M. Tarascon, *Science*, 2011, **334**, 928.
5   F. Wang, S. Xiao, Y. Hou, C. Hu. L. Liu and Y. Wu, *RSCAdv.*, 2013, **3**, 13059.
6   J. W. Long, D. Bélanger. T. Brousse, W. Sugimoto, M. B. Sassin and O. Crosnier, *MRS. Bull.,* 2011, **36**, 513.
7   R. T. Wang and X. B. Yan, *Sci.Rep.* 2014, **4**: 3712; J. T. Zhang, J. W. Jiang, H. L. Li and X. S. Zhao, *Energy Environ. Sci.*, 2011, **4**, 4009; K. B. Xu, W. Y. Li, Q. Liu, B. Li, L. An, Z. G. Chen, R. J. Zou and J. Q. Hu, *J. Mater. Chem. A*, 2014,**2**, 4795; X. Wang, A. Sumboja, J. Yan and P. S. Lee, *Nanoscale*, 2012,**4**, 7266.
8   Z. Fan, J. Yan, T. Wei, L, Zhi, G. Ning, T. Li and F. Wei, *Adv. Funct. Mater.*, 2011, **21**, 2366.
9   Y. W. Cheng, H. B. Zhang, S. T. Lu, C. V. Varanasi and J. Liu, *Nanoscale,* 2013, **5**, 1067.
10   Y. Liu, B. Zhang, Y. Yang, Z. Chang, Z. Wen and Y. Wu, *J. Mater. Chem. A*, 2013, **1**, 13582.
11   L. T. Lam and R. Louey, *J. Power Sources*, 2006, **158**, 1140.

12 D. W. Wang, F. Li and H. M. Cheng, *J. Power Sources*, 2008, **185**, 1563; H. W. Wang, H. Yi and X. F. Wang, *J. Mater. Chem. A*, 2014, **2**, 3223; F. Luan, G. Q. Wang, Y. C. Ling, X. H. Lu, H. Y. Wang, Y. X. Tong, X. X. Liu and Y. Li, *Nanoscale*, 2013, **5**, 7984; B. Wang, J. S. Chen, Z. Y. Wang, S. Madhavi and X. W. Lou, *Adv. Energy Mater.*, 2012, **2**, 1188.

13 L. B. Kong, M. Liu, J. W. Lang, Y. C. Luo and L. Kang, *J. Electrochem. Soc.*, 2009, **156**, A1000.

14 H. B. Li, M. H. Yu, F. X. Wang, P. Liu, Y. Liang, J. Xiao, C. X. Wang, Y. X. Tong and G. W. Yang, *Nat. Commun.*, 2013, **4**: 1894; J. Yan, W. Sun, T. Wei, Q. Zhang, Z. J. Fan and F. Wei, *J. Mater. Chem.*, 2012, **22**, 11494.

15 L. Demarconnay, E. Raymundo-Piñero and F. Béguin, *J. Power Sources*, 2011, **196**, 580; M. K. Liu, W. W. Tjiu, J. S. Pan, C. Zhang, W. Gao and T. X. Liu, *J. Mater. Chem. A*, 2014, DOI: 10.1039/C3NR06650A; S. H. Yang, X. F. Song, P. Zhang and L. Cao, *J. Mater. Chem. A*, 2013, **1**, 14162; S. S. Wu, W. F. Chen and L. F. Yan, *J. Mater. Chem. A*, 2014, **2**, 2765-2772; W. J. Chen, Y. M. He, X. D. Li, J. Y. Zhou, Z. X. Zhang, C. H. Zhao, C. S. Gong, S. K. Li, X. J. Pan and E. Q. Xie, *Nanoscale*, 2013, **5**, 11733.

16 W. Tang, L. Liu, S. Tian, L. Li, Y. Yue, Y. Wu and K. Zhu, *Chem. Commun.*, 2011, **47**, 10058; Y. Liu, B. H. Zhang, Y. Q. Yang, Z. Chang, Z. B. Wen and Y. P. Wu, *J. Mater. Chem. A*, 2013, **1**, 13582.

17 W. Tang, H. Hou, F. Wang, L. Liu, Y. Wu and K. Zhu, *Nano Lett.*, 2013, **13**, 2036.

18 F. Wang, S. Xiao, Z. Chang, Y. Yang and Y. Wu, *Chem. Commun.*, 2013, **49**, 9209.

19 M. Zhao, G. Huang, B. Zhang, F. Wang and X. Song, *J. Power Sources*, 2012, **211**, 202.

20 Y. Hou, X. Wang, Y. Zhu, C. Hu, Z. Chang, Y. Wu and R. Holze, *J. Mater. Chem. A*, 2013, **1**, 14713.

21 Z. H. Gao, H. Zhang, G. P. Cao, M. F. Han and Y. S. Yang, *Electrochim. Acta*, 2013, **87**, 375.

22 W. H. Jin, G. T. Cao and J. Y. Sun, *J. Power Sources*, 2008, **175**, 686.

23 X. Lu, M. Yu, T. Zhai, G. Wang, S. Xie, T. Liu, C. Liang, Y. Tong and Y. Li, *Nano Lett.*, 2013, **13**, 2628.

24 H. Wang, Y. Liang, T. Mirfakhrai, Z. Chen, H. S. Casalongue and H. Dai, *Nano Res.*, 2011, **4**, 729.

25 W. H. Jin, G. T. Cao and J. Y. Sun, *J. Power Sources*, 2008, **175**, 686.

26 J. Cheng, M. Jin, F. Yao, T. H. Kim, V. T. Le, H. Yue, F. Gunes, B. Li, A. Ghosh, S. Xie and Y. H. Lee, *Adv. Funct. Mater.*, 2013, **23**, 5074.

27 Z. Chen, Y. Qin, D. Weng, Q. Xiao, Y. Peng, X. Wang, H. Li. F. Wei and Y. Lu, *Adv. Funct. Mater.*, 2009, **19**, 3420; C. Z. Yuan, B. Gao and X. G. Zhang, *J. Power Sources*, 2007, **173**, 606; A. Q. Pan, H. B. Wu, L. Yu, T. Zhu and X. W. Lou, *ACS Appl. Mater. Interfaces*, 2012, **4**, 3874.

28 X. Lu, M. Yu, G. Wang, T. Zhai, S. Xie, Y. Ling, X. Tong and Y. Li, *Adv. Mater.*, 2013, **25**, 267.

29 Y. P. Lin and N. L. Wu, *J. Power Sources*, 2011, **196**, 851.

30 D. Choi, G. E. Blomgren and P. N. Kumta, *Adv. Mater.,* 2006, **18**, 1178.

31 X. Xiao, X. Peng, H. Jin, T. Li, C. Zhang, B. Gao, B. Hu, K. Huo and J. Zhou, *Adv. Mater.,* 2013, **25**, 5091.

32 E. Eustache, R. Frappier, R. L. Porto, S. Bouhtiyya, J. F. Pierson and T. Brousse, *Electrochim. Commun.*, 2013, **28**, 104.

33 C. Z. Yuan, X. G. Zhang, L. R. Hou, L. F. Shen, D. K. Li, C. G. Fan and J. M. Li, *J. Mater. Chem.,* 2010, **20**, 10809; X. L. Huang, J. Chai, T. Jiang, Y. J. Wei, G. Chen, W. Q. Liu, D. X. Han, L. Niu, L. M, Wang and X. B. Zhang, *J. Mater. Chem.*, 2012, **22**, 3404; C. Y. Yan, H. Jiang, Ting, Zhao, C. Z. Li, J. Ma, P. S. Lee, *J. Mater. Chem.*, 2011, **21**, 10482; F. Zhang, C. Z. Yuan, J. J. Zhou, J. Wang, X. G. Zhang and X. W. Lou, *Adv. Funct. Mater.*, 2013, **23**, 3909.

34 C. M. Ghimbeu, E. Raymundo-Pinero, P. Fioux, F. Beguin and C. Vix-Guterl, *J. Mater. Chem.*, 2011, **21**, 13268.

35 A. M. Glushenkov, D. Hulicova-Jurcakova, D. Lleywellyn, G. Q. Lu and Y. Chen, *Chem. Mater.*, 2010, **22**, 914.

36 D. Choi and P. N. Kumta, *Adv. Mater.*, 2006, **18**, 1178; F. Cheng, C. He, D. Shu, H. Chen, J. Zhang, S. Tang, D. E. Finlow, *Mater. Chem. Phys.*, 2011, **131**, 268; L. Zhang, C. M. B. Holt, E. J. Luber, B. C. Olsen, H. Wang, M. Danaie, X. Cui. X. Tan, V. W. Lui, W. P. Kalisvaart and D. Mitlin, *J. Phys. Chem. C*, 2011, **115**, 24381.

37 J. P. Zheng, *J. Electrochem. Soc.*, 2003, **150**, A484.

38 J. P. Zheng, *J. Electrochem. Soc.*, 2009, **156**, A500.

39 G. A. Snook, G. J. Wilson and A. G. Pandolfo, *J. Power Sources*, 2009, **186**, 216.
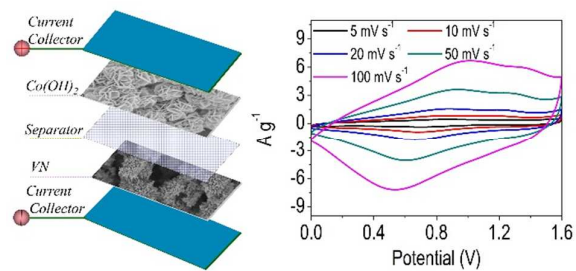
Text: A new hybrid supercapacitor with excellent electrochemical performance is fabricated by using the flower-like $Co(OH)_2$ and urchin-like VN.